

Photon counting compressive depth mapping

Gregory A. Howland,^{1,*} Daniel J. Lum,¹ Matthew R. Ware² and John C. Howell¹

¹University of Rochester Department of Physics and Astronomy, 500 Wilson Blvd, Rochester, NY 14618, USA

²Department of Physics, Campus Box 4560, Illinois State University, Normal, IL 61790, USA
[*ghowland@pas.rochester.edu](mailto:ghowland@pas.rochester.edu)

Abstract: We demonstrate a compressed sensing, photon counting lidar system based on the single-pixel camera. Our technique recovers both depth and intensity maps from a single under-sampled set of incoherent, linear projections of a scene of interest at ultra-low light levels around 0.5 picowatts. Only two-dimensional reconstructions are required to image a three-dimensional scene. We demonstrate intensity imaging and depth mapping at 256×256 pixel transverse resolution with acquisition times as short as 3 seconds. We also show novelty filtering, reconstructing only the difference between two instances of a scene. Finally, we acquire 32×32 pixel real-time video for three-dimensional object tracking at 14 frames-per-second.

© 2024 Optical Society of America

OCIS codes: (110.6880) Three-dimensional image acquisition; (110.1758) Computational imaging; (280.3640) Lidar.

References and links

1. M. C. Amann, T. Bosch, M. Lescure, R. Myllyla, and M. Rioux, "Laser ranging: a critical review of usual techniques for distance measurement," *Opt. Eng.* **40**, 10–19 (2001).
2. C. Mallet and F. Bretar, "Full-waveform topographic lidar: State-of-the-art," *ISPRS Journal of Photogrammetry and Remote Sensing* **64**, 1 – 16 (2009).
3. S. Hussmann and T. Liepert, "Three-dimensional TOF robot vision system," *IEEE Trans. Instrum. Meas.* **58**, 141–146 (2009).
4. S. Foix, G. Alenya, and C. Torras, "Lock-in time-of-flight (TOF) cameras: A survey," *IEEE Sensors J.* **11**, 1917–1926 (2011).
5. B. Schwarz, "Mapping the world in 3D," *Nat. Photonics* **4**, 429–430 (2010).
6. A. McCarthy, N. J. Krichel, N. R. Gemmell, X. Ren, M. G. Tanner, S. N. Dorenbos, V. Zwiller, R. H. Hadfield, and G. S. Buller, "Kilometer-range, high resolution depth imaging via 1560 nm wavelength single-photon detection," *Opt. Express* **21**, 8904–8915 (2013).
7. M. Richard and W. Davis, "Jigsaw: A foliage-penetrating 3D imaging laser radar system," *Lincoln Laboratory Journal* **15**, 1 (2005).
8. M. Vaidyanathan, S. Blask, T. Higgins, W. Clifton, D. Davidsohn, R. Carson, V. Reynolds, J. Pfannenstiel, R. Cannata, R. Marino, J. Drover, R. Hatch, D. Schue, R. Freehart, G. Rowe, J. Mooney, C. Hart, B. Stanley, J. McLaughlin, E. I. Lee, J. Berenholtz, B. Aull, J. Zayhowski, A. Vasile, P. Ramaswami, K. Ingersoll, T. Amoroso, I. Khan, W. Davis, and R. Heinrichs, "Jigsaw phase III: a miniaturized airborne 3-D imaging laser radar with photon-counting sensitivity for foliage penetration," *Proc. SPIE* **6550**, 65500N (2007).
9. M. Entwistle, M. A. Itzler, J. Chen, M. Owens, K. Patel, X. Jiang, K. Slomkowski, and S. Rangwala, "Geiger-mode APD camera system for single-photon 3D lidar imaging," *Proc. SPIE* **8375**, 83750-D (2012).
10. M. A. Itzler, M. Entwistle, M. Owens, K. Patel, X. Jiang, K. Slomkowski, S. Rangwala, P. F. Zalud, T. Senko, J. Tower, and J. Ferraro, "Comparison of 32 x 128 and 32 x 32 geiger-mode APD FPAS for single photon 3D lidar imaging," *Proc. SPIE* **8033**, 80330G (2011).

11. M. Duarte, M. Davenport, D. Takhar, J. Laska, T. Sun, K. Kelly, and R. Baraniuk, "Single-pixel imaging via compressive sampling," *IEEE Signal Process. Mag.* **25**, 83–91 (2008).
12. M. Sarkis and K. Diebold, "Depth map compression via compressed sensing," in *Proceedings of 16th IEEE International Conference on Image Processing*, (IEEE, 2009), pp. 737–740.
13. A. Kirmani, A. Colaço, F. N. C. Wong, and V. K. Goyal, "Exploiting sparsity in time-of-flight range acquisition using a single time-resolved sensor," *Opt. Express* **19**, 21485–21507 (2011).
14. G. A. Howland, P. B. Dixon, and J. C. Howell, "Photon-counting compressive sensing laser radar for 3D imaging," *Appl. Opt.* **50**, 5917–5920 (2011).
15. L. Li, L. Wu, X. Wang, and E. Dang, "Gated viewing laser imaging with compressive sensing," *Appl. Opt.* **51**, 2706–2712 (2012).
16. W. R. Babbitt, Z. W. Barber, and C. Renner, "Compressive laser ranging," *Opt. Lett.* **36**, 4794–4796 (2011).
17. D. L. Donoho, "Compressed Sensing," *IEEE Trans. Inf. Theory* **52**, 1289–1306 (2006).
18. E. Candès and J. Romberg, "Sparsity and incoherence in compressive sampling," *Inverse Probl.* **23**, 969 (2007).
19. M. Lustig, D. Donoho, and J. M. Pauly, "Sparse MRI: The application of compressed sensing for rapid MR imaging," *Magn. Reson. Med* **58**, 1182–1195 (2007).
20. J. Bobin, J.-L. Starck, and R. Ottensamer, "Compressed sensing in astronomy," *IEEE J. Sel. Topics Signal Process.* **2**, 718–726 (2008).
21. S. T. Flammia, D. Gross, Y.-K. Liu, and J. Eisert, "Quantum tomography via compressed sensing: error bounds, sample complexity and efficient estimators," *New J. Phys.* **14**, 095022 (2012).
22. G. A. Howland and J. C. Howell, "Efficient high-dimensional entanglement imaging with a compressive-sensing double-pixel camera," *Phys. Rev. X* **3**, 011013 (2013).
23. M. A. T. Figueiredo, R. D. Nowak, and S. J. Wright, "Gradient Projection for Sparse Reconstruction: Application to Compressed Sensing and Other Inverse Problems," *IEEE J. Sel. Topics Signal Process.* **1**, 586–597 (2007).
24. D. Donoho and I. Johnstone, "Threshold selection for wavelet shrinkage of noisy data," in *Proceedings of the 16th Annual International Conference of the IEEE Engineering in Medicine and Biology Society*, (IEEE 1994), **1** A24–A25.
25. C. Li, W. Yin, and Y. Zhang, "TVAL3: TV minimization by augmented lagrangian and alternating direction algorithms," <http://www.caam.rice.edu/~optimization/L1/TVAL3/>.
26. Z. T. Harmony, R. F. Marcia and R. F. Willett, "Sparse poisson intensity reconstruction algorithms" in *Proceedings of the IEEE/SP 15th Workshop on Statistical Signal Processing* (IEEE 2009), pp 634–637.
27. D. L. Donoho, A. Maleki, and A. Montanari, "The Noise- Sensitivity Phase Transition in Compressed Sensing", *IEEE Trans. Inf. Theory* **57**, 6920 (2011).
28. V. Cevher, A. Sankaranarayanan, M. F. Duarte, D. Reddy, R. G. Baraniuk, and R. Chellappa, "Compressive sensing for background subtraction," in *Computer Vision - ECCV 2008 Lecture Notes in Computer Science* (Springer, 2008) pp. 155–168.
29. O. S. Magaña-Loaiza, G. A. Howland, M. Malik, J. C. Howell, and R. W. Boyd, "Compressive object tracking using entangled photons," *Appl. Phys. Lett.* **102**, 231104 (2013).

1. Introduction

High-resolution three-dimensional imaging, particularly using time-of-flight (TOF) lidar, is very desirable at ultra-low light levels. Such weakly-illuminated systems are safer, require less power, and are more difficult to intercept than their high-power equivalents. Potential applications include large- and small-scale surface mapping, target recognition, object tracking, machine vision, eye-safe ranging, and atmospheric sensing [1–5].

In a TOF lidar system, a scene is illuminated by laser pulses. The pulses reflect off targets in the scene and return to a detector. Correlating the returning signal with the outgoing pulse train provides the TOF, which is converted to distance-of-flight (DOF). Transverse spatial resolution can be obtained either by scanning through the scene pixel-by-pixel or by using a detector array, such as a time-resolving CCD.

To achieve low-light capability, many recent efforts use photon-counting detectors for the detection element(s). Such detectors provide shot-noise limited detection with single-photon sensitivity and sub-ns timing. Examples include established technologies such as photo-multiplier tubes and geiger-mode avalanche photo-diodes (APDs), as well as more experimental devices such as superconducting nano-wires [6].

While they provide exceptional sensitivity and noise performance, photon-counting systems are challenging to scale to high transverse resolution. Systems that scan a single-element de-

tector benefit from mature technology, but suffer from acquisition times linearly proportional to the spatial resolution. Significant per-pixel dwell times limit real-time performance to low resolution.

Alternately, researchers have constructed photon counting detector arrays, such as that used by MIT Lincoln Labs JIGSAW [7,8] and its successors [9]. Fabrication difficulties limit sensor sizes to a current-best resolution of 32×128 pixels, with 32×32 pixels available commercially [10]. These sensors suffer from high dark count rates, pixel cross-talk, and significant readout noise. For TOF ranging, each pixel must be simultaneously correlated with the pulse train, a resource intensive process.

The goal is to overcome these challenges without increasing system cost and complexity. A promising option uses a standard, single-element, photon counting detector as the detection element in a compressive sensing, single-pixel camera [11]. The single-pixel camera leverages a scene’s compressibility to recover an image from an under-sampled series of incoherent projections. This is accomplished by imaging the scene onto a sequence of psuedo-random patterns placed on a spatial light modulator (SLM) or digital micro-mirror device (DMD). The inner-product of the scene and pattern is measured by a single-element, “bucket” detector. Optimization routines then recover the image from many fewer projections than pixels, often less than 10 percent.

The single-pixel camera can be adapted for TOF depth mapping by switching to active, pulsed illumination. Standard CS techniques require measurements to be linear projections of the signal of interest. Unfortunately, in a TOF single-pixel camera, the depth map is non-linearly related to the acquired measurements, as they contain both depth and intensity information [12, 13]. Current approaches mitigate or altogether avoid this issue in various ways. In 2011, we presented a proof-of-principle lidar camera where CS is used only to acquire transverse information [14]. Range is determined by gating on a TOF of interest. This reduces to the conventional single-pixel camera problem, but requires separate reconstructions for each depth of interest. Li et. al. present a similar, gated system (GVLICS) that recovers 3D images [15]. Kirmani et. al. [13] introduce a more sophisticated protocol (CoDAC) that incorporates parametric signal processing and a reconstruction process exploiting sparsity directly in the depth map. This system uses intermediate optimization steps to keep the problem linear.

CS can also be applied directly in the time-domain, and has been proposed for non-spatially resolving lidar systems [16]. In principle, one could combine this with transverse CS for a full 3D voxel reconstruction. This signal is extremely high dimensional and presents substantial measurement and reconstruction challenges.

In this manuscript, we present an alternative single-pixel camera adaptation for photon-counting depth mapping and intensity imaging. Rather than recover the depth map directly, we separately recover an intensity map and an intensity \times depth map, where the depth map is simply their ratio. Linear projections of these signals are easily acquired using a TOF single-pixel camera with a photon counting detection element, with available light levels around 0.5 picowatts. Our approach is straightforward and uses standard CS formulations and solvers. We demonstrate imaging at resolutions up to 256×256 pixels with practical acquisition times as low as 3 seconds. We also show novelty filtering; finding the difference between two instances of a scene without recovering the full scenes. Finally, we demonstrate video acquisition and object tracking at 32×32 pixel resolution and 14 frames per second.

2. Compressive Sensing

2.1. Introduction to CS

Compressive sensing [17] is a measurement technique that uses optimization to recover a sparsely represented, n -dimensional signal X from $m < n$ measurements. CS exploits a signal’s

compressibility to require fewer measurements than the Nyquist limit. The detection process can be modeled by interacting X with a $m \times n$ sensing matrix A such that

$$Y = AX + \Gamma, \quad (1)$$

where Y is a m -dimensional vector of measurements and Γ is a m -dimensional noise vector. Because $m < n$, and rows of A are not necessarily linearly independent, a given set of measurements does not specify a unique signal.

To recover the correct signal, CS formulates an objective function to select the sparsest X consistent with the measurements:

$$\min_X \frac{1}{2} \|Y - AX\|_2^2 + \tau g(X), \quad (2)$$

where τ is a scaling constant between penalties. The first penalty is a least-squares term that ensures the signal matches the measured values. The second penalty, $g(X)$, is a sparsity-promoting regularization function. Typical $g(X)$ include the ℓ_1 norm of X or the total variation of X . For a k -sparse signal (only k significant elements), exact reconstruction is possible for $m \propto k \log(n/k)$ measurements. In practice, m is often only a few percent of n . For minimum m , the sensing matrix must be incoherent with the sparse basis, with the counter-intuitive result that random, binary sensing vectors work well [18].

2.2. Single-pixel Camera

The quintessential application of CS is the single-pixel camera [11]. Duarte et. al. cleverly implemented an incoherent sensing matrix by imaging a scene onto a digital micro-mirror device (DMD) of the sort found in digital movie projectors. The DMD is an array individually addressable mirrors that can be selectively oriented to reflect light either to a single-pixel “bucket” detector or out of the system. The measured intensity yields the inner-product of a pattern placed on the DMD with the scene of interest. To perform the set of measurements described in Eq. (1), pseudorandom binary patterns are placed sequentially on the DMD, where each pattern represents a row of sensing matrix A . Elements of Y are the measured intensities for corresponding patterns. An image of the scene is then recovered by an algorithm that solves Eq. (2).

CS and the single-pixel camera sparked a mini-revolution in sensing as researchers found their ideas could be easily and directly applied to common problems across a breadth of fields from magnetic resonance imaging [19] to radio astronomy [20] to quantum entanglement characterization [21, 22].

3. Compressive Depth Mapping

3.1. Adapting SPC for Depth Mapping

The single-pixel camera can be adapted for depth mapping at very low light levels by switching to active, pulsed illumination and using a photon-counting detection element. Our setup is given in Fig. 1. A scene containing targets at different depths is flood illuminated by a pulsed laser diode. The scene is imaged onto a DMD which implements an incoherent sensing matrix. Light from DMD “on” pixels is redirected to a photo-multiplier module that detects individual photon arrivals. A time-correlated single-photon counting module (TCSPC) correlates photon arrivals with the outgoing pulses to find each photon’s TOF. Full experimental specifications are given in Table 1.

Recovery of a two-dimensional, intensity only image X_I (a gray-scale image) is identical to the normal single-pixel camera. Patterns from the sensing matrix are placed sequentially on the DMD. For each pattern, the number of detected photons is recorded to obtain a measurement vector Y_I . Eq. (2) is then used to find the intensity image X_I .

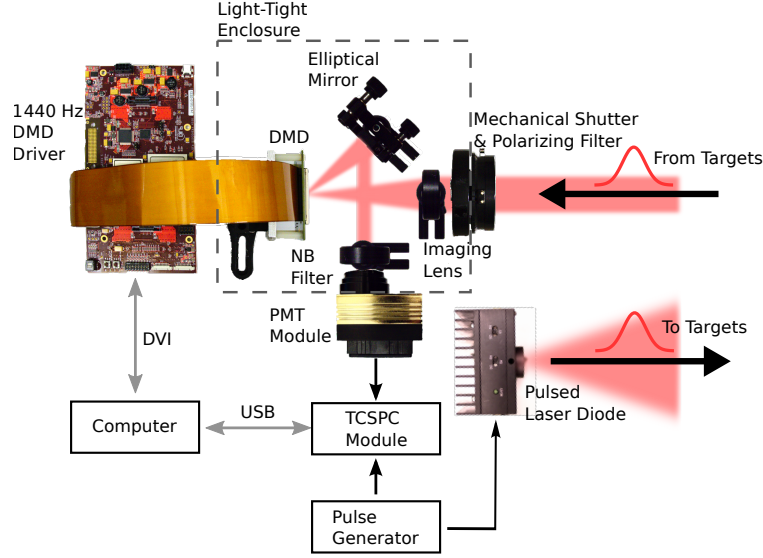


Fig. 1. **Experimental Setup** A 780 nm, 10 Mhz, 2 ns pulsed laser diode flood illuminates a scene containing targets at different depths. Returning pulses are imaged onto a DMD array with resolution up to 256×256 pixels. A polarizer prevents flares from specular reflection. Light reflecting off DMD “on” pixels is directed through a narrow-band filter to a single-photon sensitive PMT module that produces TTL pulses. Typical count rates are about 2 million photons per second. A TCSPC module time-correlates photon arrivals with the outgoing pulse train to determine a TOF for each detected photon. A series of pseudorandom, binary patterns consisting of randomly permuted, zero-shifted Hadamard patterns are placed on the DMD with per-pattern dwell times as short as $1/1440$ sec. These implement an incoherent sensing matrix. For each pattern, the number of photon arrivals and their total TOF is recorded. Our protocol is then used to reconstruct the intensity image and the depth map.

Unfortunately, recovering a depth map X_D from the TOF information is not straightforward because the measurements are nonlinear in X_D . Consider photon arrivals during one pattern. Each photon has a specific TOF, but is only spatially localized to within the sensing pattern. It is possible, and likely, that multiple photons will arrive from the same location in the scene. Individual detection events therefore contain information about both intensity and depth.

Consider the signal X_Q made up of the element-wise product $X_Q = X_I \cdot X_D$. Unlike X_D , X_Q can be linearly sampled by summing the TOF of each photon detected during the measurement. This can be seen by expanding this total TOF sum over the contribution from each pixel in the scene, such that

$$Y_Q = AX_Q = \left\{ C \sum_{j=1}^N A_{ij} \eta_j T_j \right\} \text{ for } i = 1 \text{ to } m, \quad (3)$$

where i is an index over sensing patterns and j is an index over all DMD pixels. A_{ij} is the DMD status (0 or 1) of pixel j during the i^{th} pattern, η_j is the number of photons reaching pixel j during the measurement, and T_j is the TOF of a photon arriving at pixel j . C is a constant factor converting photon number to intensity and TOF to depth. Each pixel where $A_{ij} = 1$ (the DMD mirror is “on”) contributes $\eta_j T_j$ to the TOF sum for pattern i . This is a product of an intensity (photon number) and a depth (TOF). X_Q is therefore equal to $C\eta \cdot T$. Because Eq. (3) takes the

form of Eq. (1), Eq. (2) is suitable for recovering X_Q .

The depth map is simply the element-wise division of X_Q by X_I . Note that Y_I and Y_Q are acquired simultaneously from the same signal; Y_I represents that number of photon arrivals for each pattern and Y_Q is the sum of photon TOF for each pattern. The only increase in complexity is that two optimization problems must now be solved, but these are the well understood linear problems characteristic of CS.

3.2. Protocol

A slightly more sophisticated approach including noise reduction vastly improves practical performance. The protocol we use for depth map recovery is as follows:

1. Acquire measurement vectors $Y_Q = AX_Q$ and $Y_I = AX_I$, where $X_Q = X_I.X_D$.
2. Use sparsity maximization routine (Eq. (2)) on Y_Q to recover noisy \bar{X}_Q .
3. Apply hard thresholding to \bar{X}_Q . The subset of non-zero coefficients in a sparse representation of \bar{X}_Q now form an over-determined, dense recovery problem.
4. Perform a least squares debiasing routine on non-zero coefficients of \bar{X}_Q in the sparse representation to find their correct values and recover X_Q .
5. Take significant coefficients of X_I to be identical to X_Q . Perform the same least squares debiasing on these coefficients of X_I .
6. Recover X_D by taking $\text{Nz}(X_I).X_Q./X_I$, where $\text{Nz}(x) = 1$ for non-zero x and 0 otherwise.
7. (optional) In the case of very noisy measurements, perform masking on X_D and X_I .

First, we acquire measurement vectors Y_I and Y_Q as previously described. Rather than independently solve Eq. (2) for both measurement vectors, we only perform sparsity maximization on Y_Q . In practice, solvers for Eq. (2) tend to be more effective at determining significant coefficients than finding their correct values, particularly given noisy measurements [23]. We therefore rely on sparsity maximization only to determine which coefficients are significant. We subject the noisy, recovered \bar{X}_Q to uniform, hard thresholding [24] in a sparse representation, which forces the majority of the coefficients to zero. The sparse basis is typically wavelets, but may be the pixel basis for simple images.

The subset of coefficients remaining after thresholding is considered significant. If only these coefficients are considered, the problem is now over-determined and a least-squares debiasing routine is applied to find their correct values and yield the signal X_Q [23]. We assume the significant coefficients for X_I are the same as for X_Q , and apply least-squares debiasing to X_I as well. Finally, we recover the depth map X_D by taking

$$X_D = \text{Nz}(X_I).X_Q./|X_I| \quad (4)$$

where $\text{Nz}(p) = 1$ for nonzero p and 0 otherwise. This prevents a divide-by-zero situation when an element of $X_I = 0$, meaning no light came from that location.

For very noisy measurements, the sparsity maximization in steps 2-3 gives accurate outlines for targets in the scene, but poorly recovers pixel values. After the least squares debiasing in steps 4 and 5, values are more accurate, but the outlines can become distorted. A best-of-both-worlds solution is to threshold the result of step 4 in the pixel basis to create a binary object mask. This mask can optionally be applied to the final X_I and X_D for spatial clean up.

Table 1. System Specifications

Parameter	Comments
Laser	Laser Diode mounted in Thorlabs TCLDM9
Repetition Rate	10 MHz
Pulse Width	2 ns = 60 cm
Wavelength	780 nm
Average Output Power	4 mW
Average Detected Power	0.5 pW (2 megacounts per second)
Spectral Filters	780/10 nm Bandpass, Optical Depth 6+
DMD Device	Digital Light Innovations D4100 with 1024×768 DMD, operated in binary expansion mode at 1440 frames per second
Spatial Resolution	images: 256×256 pixels video: 32×32 pixels
Detector	Horiba TBX-900C Photomultiplier Module with 9 mm^2 active area
Jitter	$< 200 \text{ ps}$
Dark Count Rate	< 200 counts per second
Data Acquisition	PicoQuant PicoHarp 300 operating in time-tagging mode
Imaging Lens Focal Length	75 mm

4. Experimental Setup

Our experimental setup is given in Fig. 1, with specifications given in Table 1. Targets are flood illuminated with 2 ns, 780 nm laser pulses with a 10 MHz repetition rate. Average illumination power is 4 mW. The scene is imaged onto a DMD array, where on pixels are redirected through a 780/10 nm bandpass filter to a photon-counting photo-multiplier module. A sequence of m sensing patterns are displayed on the DMD at 1440 Hz. For each pattern, the number of photon arrivals and the sum of photon TOF is recorded. If $1/1440$ seconds is an insufficient per-pattern dwell time t_p , the pattern sequence is repeated r times so that $t_p = r/1440$ and the total exposure time t is $t = mt_p = mr/1440$. The average detected photon rate is 2 million counts per second, or 0.5 picowatts.

Sensing vectors (patterns) are randomly selected rows of a zero-shifted, randomly-permuted Hadamard matrix. The Hadamard transform matrix is closely related to the Fourier transform matrix, but entries only take real values 1 or -1 . The zero shifted version sets all -1 values to zero. When randomly permuted, they make practical sensing vectors because repeated calculations of AX in the reconstruction algorithms can be computed via fast transform. This is computationally efficient because the fast transform scales logarithmically and the sensing matrix does not need to be stored in memory [25].

The sparsity promoting regularization is either the signal's ℓ_1 norm or total variation depending on the scene and exposure time. For ℓ_1 minimization, we use a gradient projection solver [23]. For TV minimization, We use the TVAL3 solver [25]. The sparse representation

for wavelet thresholding and least-squares debiasing is Haar Wavelets. Higher order Daubechies wavelets were tested, but did not significantly improve results for test scenes presented in this manuscript. They may offer improvements for more complicated scenes in future work.

Processing times for reconstructions vary based on transverse resolution, scene complexity, and noise. Test scenes in this manuscript were recovered either at resolutions of $n = 256 \times 256$ or $n = 32 \times 32$. A 256×256 reconstruction consistently took less than 5 minutes, while a 32×32 reconstruction took less than 5 seconds. The solvers and supporting scripts are implemented in Matlab, with no particular emphasis on optimizing their speed. The majority of computational resources are used for performing Fast Hadamard Transforms and reading and writing large files. If more efficient file formats are used, and the Fast Hadamard Transform is computed on a GPU or DSP, reconstruction speeds approach real-time.

4.1. Noise Considerations

While an exhaustive noise analysis is beyond the scope of this manuscript and a subject of future work, some important qualitative aspects should be explored. There are two dominant sources of error in the measurements of Y_I and Y_Q . The first is simply shot noise, a fundamental uncertainty in number of measured photons limiting the measured SNR to $\sqrt{\eta}$ for η detected photons. Because incoherent measurements used for compressive sensing use half the available light on average, the information they convey is contained in their deviation from the mean. As a general rule, a successful reconstruction requires the standard deviation of the measurement vector to exceed the shot noise. Compressive sensing has been shown to work well in the presence of shot noise in comparison to other sensing methodologies. For more information see Refs. [11, 26, 27].

The other primary error sources are detector dark counts and ambient light. All photon-counting detectors have the possibility of firing without absorbing a photon. For a particular detector, these events occur at some rate and the timing is uniformly distributed. For a statistically significant acquisition time, the dark counts simply add constant values to both Y_Q and Y_I . These values can be easily measured by blocking the detector and observing count rates in the absence of signal. They can then be subtracted from future measurement vectors.

Ambient light is also uncorrelated with the pulsed illumination, so ambient photon arrivals are uniformly distributed. If the ambient light is spatially uniform, it adds a constant value to both Y_Q and Y_I because half the DMD pixels are always directed to the detector. If the ambient light is not spatially uniform, the contribution may be different for different sensing patterns. In either case, m -dimensional ambient vectors \mathcal{A}_Q and \mathcal{A}_I can be obtained by disabling the pulsed laser and performing the measurements normally used to obtain Y_Q and Y_I . These can then be subtracted from Y_Q and Y_I to ameliorate the ambient light. This will also remove the dark counts.

If the ambient light is spatially uniform, the addition of a second detector which measures light from DMD “off” pixels can also mitigate the ambient light. In this case, it is no longer necessary to use zero-shifted sensing patterns, they can instead consist of values “1”, which are directed to the “on” pixel detector, and “-1”, which are directed to the “off” pixel detector. The sensing vector corresponding to this matrix is just the difference between sensing vectors obtained by each individual detector. Because each detector receives the same amount of ambient light, it will be subtracted out.

The best way to mitigate unwanted detection events is to avoid them altogether. A massive advantage of single-pixel camera technology is the ability operate at wavelengths where detector arrays are difficult to fabricate, such as the infrared. For the active, narrowband sources used in lidar systems, high optical-density, narrow-band filters can reject the vast majority of unwanted light. Our system received less than 100 dark counts per second and approximately

1000 counts per second from ambient light. With over 10^6 signal counts per second, these negligibly effected our results and the amelioration schemes discussed were not needed. They are likely to become important in more real-world applications beyond the laboratory.

5. Results

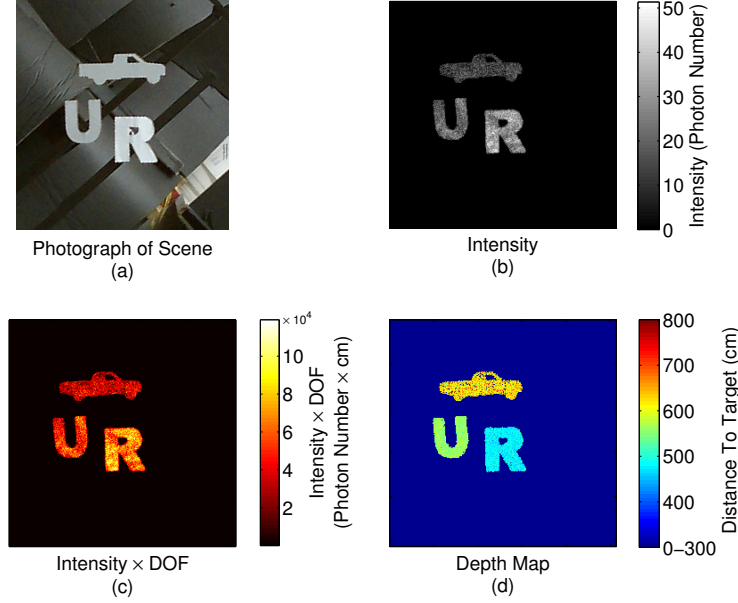


Fig. 2. **Long Exposure** A scene consisting of cardboard cutouts (a) is imaged at $n = 256 \times 256$ resolution from $m = 0.2n$ random projections with a 6.07 minute exposure time. The protocol recovers a high quality intensity map (b) and intensity \times DOF map (c). Their ratio is the depth map (d).

5.1. Simple Scene

The first test case is a simple scene containing cardboard cutouts of the letters “U” and “R” as well as the outline of a truck. The objects were placed at to-target distances of 480 cm, 550 cm, and 620 cm respectively. Fig. 2 shows a high quality reconstruction with resolution $n = 256 \times 256$ pixels, $m = 0.2n = 13108$, and $t_p = 40/1440$ for an exposure time of 6.07 minutes. The sparsity promoter was TV. Both the intensity and depth map are accurately recovered.

Pictures of the same scene with much shorter acquisition times are given in Fig. 3. Fig. 3(a) and 3(b) show the intensity and depth map for $m = 0.1n = 6554$ and $t_p = 5/1440$ seconds for a total exposure time of 23 seconds. Fig. 3(a) and 3(b) gives results for a exposure with $m = .07n = 4558$ and $t_p = 1/1440$ seconds for a total exposure time of 3 seconds. The optional masking process (protocol step 7) was used. While the reconstructions are considerably noisier than the long exposure case, the objects are recognizable and the average depths are accurate.

Note that the shortest dwell-time per pattern for the DMD is $1/1440$ sec. To raster scan at this speed for $n = 256 \times 256$ pixels would require 46 seconds, so both results in Fig. 3 are recovered faster than it is possible to raster scan. If the same dwell times were used ($t_p = 5/1440$ and $t_p = 1/1440$ seconds respectively), the raster scan would take about 228 seconds and 46 seconds. Note that many significant pixels in the recovered intensity images in Fig. 3 have less

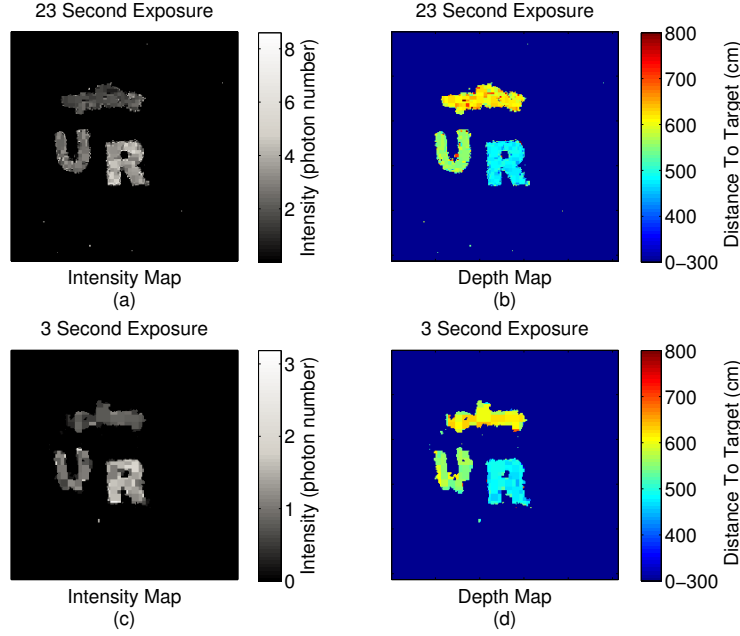


Fig. 3. **Short Exposure** Scene from Fig. 2 acquired with rapid acquisition times. The intensity and depth maps in (a) and (b) were acquired in 23 seconds while (c) and (d) were acquired in only 3 seconds. At these exposure times, the intensity map regularly contains less than one photon per significant pixel, so it is impossible to raster scan.

than 1 photon per pixel. Therefore, even the longer raster scans would struggle to produce a good picture because they cannot resolve fewer than 1 photon per pixel. Our protocol is more efficient because each incoherent projection has flux contributed from many pixels at once, measuring half the available light on average.

A generalization of the raster scan is the basis scan, a scan through basis vectors of an alternative signal representation (such as a Hadamard decomposition). The hardware in most lidar systems is based on either a detector array or raster scanning, so it is not suitable for performing a basis scan. However, with specialized equipment, such as the DMD in our setup, basis scanning is possible. Basis scanning still requires n measurements, so the minimum possible acquisition time ($t_p = 1/1440$ seconds) is the same as for raster scanning, in this case $n \times t_p = 46$ seconds. However, a basis scan using Hadamard patterns benefits from the same increased flux per measurement as the incoherent projections of CS, so SNR is improved over raster scanning. Nevertheless, CS has been shown to outperform basis scan with fewer measurements. Since the two schemes require the same hardware, CS is preferred. For a comparison of CS with other sensing techniques, including raster and basis scan, see Ref. [11].

5.2. Natural Scene

A $n = 256 \times 256$ pixel measurement of a more complicated scene containing real objects is given in Fig. 4. The scene consists of a small cactus, a shoe, and a microscope placed at to-target distances of 465 cm, 540 cm, and 640 cm respectively. A photograph of the scene is given in Fig. 4(a). The scene was acquired with $m = 0.3n$ a per-pattern dwell time $t_p = 50/1440$ seconds for an exposure time of 11.37 minutes. The sparsity promoter was the ℓ_1 norm in the Haar wavelet representation.

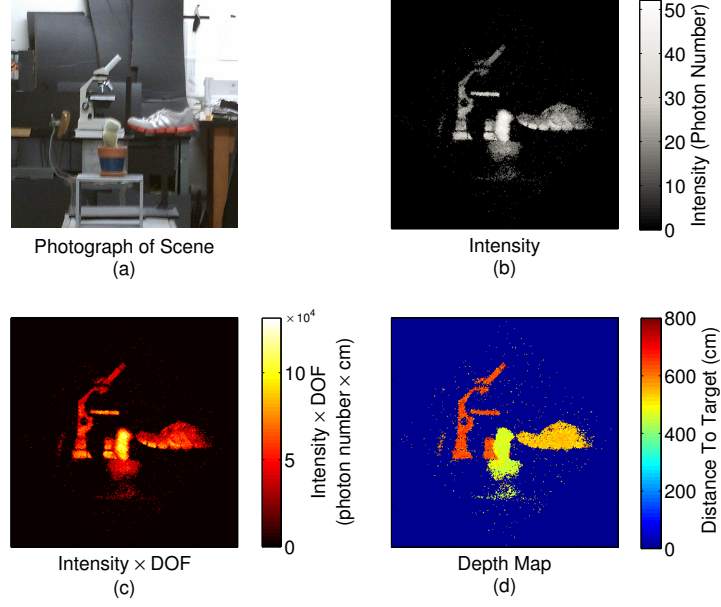


Fig. 4. **Natural Scene** A scene consisting of a cactus, shoe, and microscope is imaged at $n = 256 \times 256$ pixel resolution with $m = 0.3n$ and a per-pattern dwell time $t_p = 50/1440$ seconds.

Fig. 4(b), Fig. 4(c), and Fig. 4(d) show the reconstructed intensity, intensity \times DOF, and depth map respectively. All objects are recognizable and the to-target distances are accurately recovered. Noise is slightly higher than the simpler scene of cardboard cutouts.

5.3. Depth Calibration

The photon TOF measured by the TCSPC module is trivially converted to DOF by multiplying by speed of light c . This DOF includes the round trip distance traveled by illuminating pulses as well as delays introduced by cables and electronics. The actual distance to target is linearly related to the measured DOF.

To determine this relationship and probe the system's depth accuracy, we took images of a simple square, white, cardboard cutout placed a known distance from the camera. The cutout was sequentially moved away from the camera in small increments and the reconstructed depths were recorded.

Results are given in Fig. 5. Fig. 5(a) shows a photograph of the object, with a typical reconstructed depth map given in Fig. 5(b). Fig. 5(c) shows a coarse grained result when the object was moved in 15.25 cm (6 in) increments over a 259 cm (108 in) range. Each measurement was performed at 32×32 pixel transverse resolution with $m = 0.1n = 102$. The per-pattern dwell time was $1/1440$ seconds, so each depth map was acquired in .07 seconds. The pulse length was 2 ns, or 60 cm.

Fig. 5(c) provides the reconstructed DOF as function of the distance to object. The measured DOF is averaged over the recovered object. A linear fit shows very good agreement with the measurements, with a slope of 1.91. This is slightly less than the expected 2 (for a round-trip flight) because the result includes cable transit times. Fit error bars represent a 95% confidence interval.

We performed an additional fine resolution set of measurements where the object was moved

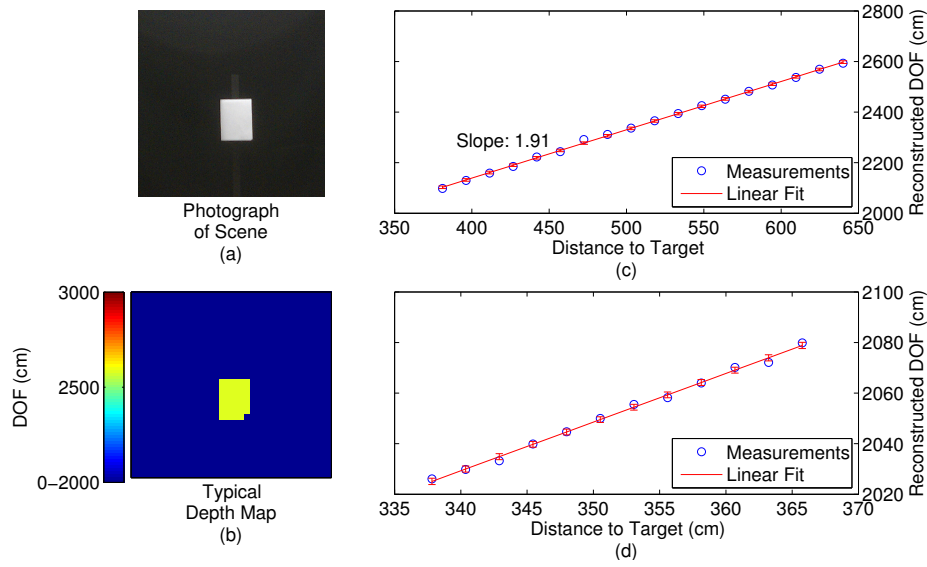


Fig. 5. **Depth Calibration** Depth maps of a rectangular cardboard cutout (a) are acquired at $n = 32 \times 32$ pixel resolution with a typical reconstruction given in (b). The cutouts to-target distance was increased in increments of 15.52 cm (c) and 2.54 cm (d). Depths can accurately recovered to less than 2.54 cm for this scene.

in 2.54 cm (1 in) increments over a 30.4 cm (12 in) range. All other parameters are identical to the coarse measurements. Results are shown in Fig. 5(d). Despite 60 cm pulse lengths, depth mapping is accurate to less than 2.54 cm. While uncertainty is slightly larger than the coarse case, the fits agree to within the confidence interval.

5.4. Novelty Filtering

For many applications such as target localization, high frame-rate video, and surveillance, it is useful to look at the difference between realizations of a scene at different times. Such novelty filtering removes static clutter to reveal changes in the scene. This is traditionally accomplished by measuring the current signal $X^{(c)}$ and subtracting from it a previously acquired reference signal $X^{(r)}$ to find $\Delta X = X^{(c)} - X^{(r)}$.

Compressive sensing is particularly well suited for novelty filtering because the difference signal ΔX can be directly reconstructed [28, 29]. Consider acquiring incoherent measurement vectors for both $X^{(r)}$ and $X^{(c)}$ as in Eq. (1), using the same sensing matrix A for both signals. Instead of separately solving Eq. (2) for each signal, first difference their measurement vectors to find

$$\Delta Y = Y^{(c)} - Y^{(r)} \quad (5)$$

$$\Delta Y = A \Delta X. \quad (6)$$

Because Eq. (6) has the same form as Eq. (1), the optimization routine can be performed directly on ΔY to obtain ΔX without ever finding $X^{(c)}$ or $X^{(r)}$. Furthermore, the requisite number of measurements m depends only on the sparsity of ΔX . For small changes in a very cluttered scene, the change can be much sparser than the full scene. It is often possible to recover the

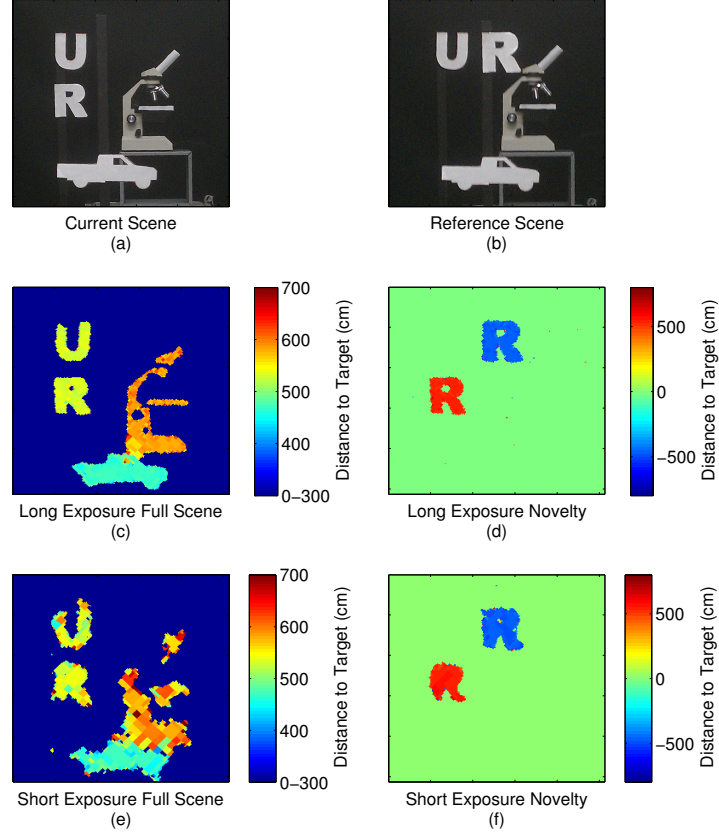


Fig. 6. **Novelty Filtering** (a) and (b) give photographs of two instances of a scene, where the 'R' has changed positions (including depth). (c) and (d) show high quality, long 6.07 minute exposure depth map reconstructions for the full current scene and difference image respectively. (e) and (f) show corresponding short 37 second exposure depth map reconstructions. Negative values in the difference image indicate the object's former location.

novelty with too few measurements to reconstruct the full scene.

Fig. 6 gives an example of using our system for novelty filtering in intensity and depth. A photograph of a current scene containing several objects is shown in 6(a). Fig. 6(b) photographs a prior reference scene. In the current scene, the cardboard cutout 'R' has been moved, both transversely and from a range of 480 cm to a range of 560 cm.

Fig. 6(c) and 6(d) give long exposure reconstructions of the full current depth map and the difference depth map respectively. Exposure parameters were $n = 256 \times 256$ pixels, $m = 0.2n$, and $t_p = 40/1440$ sec for an exposure time $t = 6.07$ minutes. The sparsity promoter was TV. The difference reconstruction contains only the 'R' object that moved. Note that there are two copies of the 'R'. One is negative, indicating the objects former position, and one is positive, indicating the objects new position.

Fig. 6(e) and 6(f) show short exposure reconstructions for the current scene and the difference image. The number of measurements was reduced to $m = 0.02n = 1311$ with $t_p = 40/1440$ for an exposure time of 37 seconds. Masking was performed. For this acquisition time, the static clutter is very poorly imaged and is difficult to recognize in the full scene. The difference image effectively removes the clutter and gives a recognizable reconstruction of the novelty.

Again, this is far faster than raster-scanning, which requires at least two 45 second scans for differencing.

5.5. Video and Object Tracking

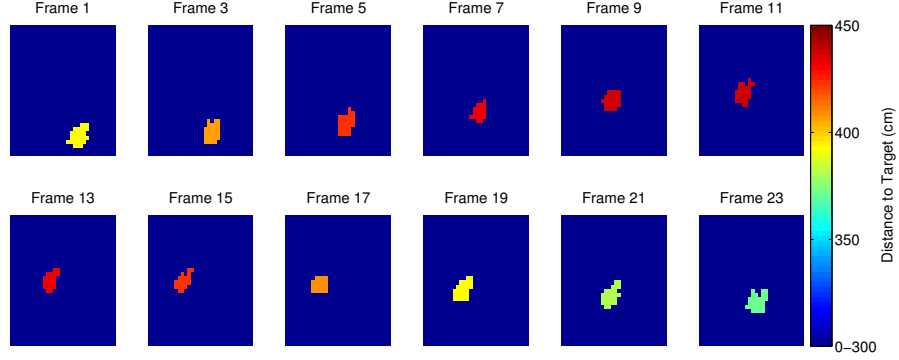


Fig. 7. **Movie** Frames from a depth-map movie ([Media 1](#)), of a three-dimensional pendulum consisting of a baseball suspended by a 170 cm rope swinging through a 25 degree solid angle. The transverse resolution is 32×32 pixels with a frame rate of 14 frames per second.

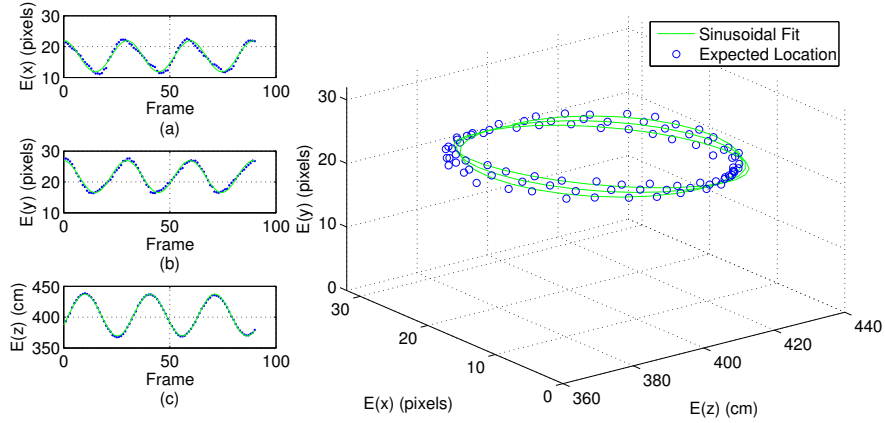


Fig. 8. **Object Tracking** The expected values for transverse (x,y) and range (z) coordinates are given in (a), (b), and (c) as a function of frame number. Blue circles show expected values obtained from reconstructed depth maps, while green lines give sinusoidal fits. (d) shows a 3D parametric plot of the pendulum's trajectory.

At lower spatial resolution, the system is capable of video and object tracking. To demonstrate this, we acquired video at 32×32 pixel resolution of a three-dimensional pendulum consisting of a baseball suspended from the ceiling by a rope. The lever arm was 170 cm and the pendulum oscillated through a solid angle of approximately 25 degrees. The three dimensions are not oscillating in phase, so the trajectory is elliptical.

Movie frames were acquired with $m = 0.1n = 99$ with a per-pattern dwell time $t_p = 1/1440$ sec. Each frame required .07 sec to acquire for a frame rate slightly exceeding 14 frames per second. The sparsity promoter was TV . Sample frames showing the pendulum moving through

a single period are given in Fig. 7, where alternate frames are skipped for presentation. We clearly recover images of the pendulum oscillating in all three dimensions. The full movie can be viewed online ([Media 1](#)).

The pendulum’s position can be tracked by taking expected values for its transverse location and averaging over its range to determine a to-target distance. Fig. 8 shows the computed pendulum trajectory. Figs 8(a), 8(b) and 8(c) give the expected x , y and z values for pendulum location as a function of frame number. These can be combined to yield the three-dimensional, parametric trajectory given in Fig. 8(d). Sinusoidal fits are in good agreement with the expected values, particularly in the depth dimension.

6. Protocol Trade-offs and Limitations

The strength of our protocol lies in its simplicity; the well-known single-pixel camera can be adapted for ranging by simply adding a pulsed source. All the standard, linear CS techniques are otherwise used. This is because our protocol treats X_Q as an image itself. Our technique is also very natural for photon counting as per-photon TOF is easy to measure and sum. However, this ease-of-use does come with some potential trade-offs.

Our protocol does not consider sparsity in the depth map itself. Depth maps have been shown to generally be sparser than intensity images [13]. Protocols which directly recover the depth map, such as in Ref. [13], can leverage this sparsity to require fewer measurements. Because incoherent measurements are nonlinear in the depth map, this comes at the cost of more complex measurement and reconstruction schemes.

In our protocol, X_Q is treated like an image. This is reasonable because it is simply a scaling of the intensity map by the depth map; it maintains much of the structure of an image and still qualitatively appears like an image to a viewer. Because X_Q is treated like an image, we use sparsity maximizers common for images such as wavelets and total variation. In these representations, X_Q is likely to be more complex (less sparse) than X_I , so the complexity of X_Q is a limiting factor reducing the number of measurements. It is possible that other representations may be more appropriate for X_Q . A full analysis of the complexity of X_Q and its absolute best representation remains an open problem.

Characteristics of the laser pulse, such as its width and shape, are also not included in the protocol. Incorporating these in the optimization may improve range resolution at the cost of a more complex objective function. The current system can accurately discriminate between objects placed less than a pulse width apart, but this discrimination breaks down as the relative photon TOF between objects becomes ambiguous. This is acceptable for many ranging tasks, but very high range resolution depth mapping may require improvements.

Finally, our objective Eq. (2) uses the standard least squares penalty to ensure reconstructions are consistent with measurements. At very low photon numbers, where the Poissonian photon number distribution deviates markedly from Gaussian statistics, a logarithmic penalty gives superior performance but requires different solvers [26]. Data sets used in this manuscript typically averaged thousands of photons per measurement, so this was a non-issue. This change would be critical if photon numbers approached single-digits per measurement.

Ultimately, increased complexity in the protocol must be weighed against potentially diminishing returns. In its current form, our protocol demonstrates most of the benefits CS provides over standard techniques. We do not claim the scheme is fundamentally optimal; rather it is a practical approach that also provides a new perspective on the compressive depth mapping problem.

7. Conclusion

We demonstrate a simple protocol for extending the single-pixel camera to time-of-flight depth mapping with a photon counting detector. Our approach requires only linear measurements so standard compressive sensing techniques can be used. The photon-counting detector allows us to work at sub-picowatt light levels. We show imaging 256×256 pixel resolution with practical acquisition times. By differencing random projections of two instances of a scene, we directly recover novelty images to efficiently remove static clutter and show only changes in a scene. We also acquire 32×32 pixel video at 14 frames per second to enable accurate three-dimensional object tracking. Our system is much easier to scale to high spatial-resolution than existing photon-counting lidar systems without increased cost or complexity.

Single-pixel camera type devices are very flexible because operational parameters can easily be changed just by switching detectors. While our proof-of-principle system operates in the lab at 780 nm, it could adapt to infrared by switching to InGaAs APDs or superconducting nanowire detectors [6]. If faster acquisition times are needed, one could use linear mode detectors or sum the output from multiple photon-counting detector. Hyperspectral imaging is possible with a frequency sensitive detector. Our protocol is a simple, effective way to add high resolution depth mapping to many low-light sensing applications.

We acknowledge support from AFOSR grant FA9550-13-1-0019 and DARPA DSO InPho grant W911NF-10-1-0404.